www.sciencemag.org/content/350/6267/1513/suppl/DC1

Supplementary Materials for

Synthesis of borophenes: Anisotropic, two-dimensional boron polymorphs

Andrew J. Mannix, Xiang-Feng Zhou, Brian Kiraly, Joshua D. Wood, Diego Alducin, Benjamin D. Myers, Xiaolong Liu, Brandon L. Fisher, Ulises Santiago, Jeffrey R. Guest, Miguel Jose Yacaman, Arturo Ponce, Artem R. Oganov,* Mark C. Hersam,* Nathan P. Guisinger*

*Corresponding author. E-mail: nguisinger@anl.gov (N.P.G.); m-hersam@northwestern.edu (M.C.H.); artem.oganov@stonybrook.edu (A.R.O.)

Published 18 December 2015, *Science* **350**, 1513 (2015)
DOI: 10.1126/science.aad1080

This PDF file includes:

Materials and Methods

Materials

Growth and *in situ* experiments were conducted in a commercial ultrahigh vacuum (UHV) system (base pressure ~10^{-11} mBar) equipped with a preparation chamber, low-energy electron diffraction (LEED), Auger electron spectroscopy (AES), and scanning tunneling microscopy (STM). Borophene was grown on single crystal Ag(111) substrates (Mateck, 99.999%), which were cleaned *via* repeated cycles of Ar sputtering followed by annealing at 550 °C. During growth, samples were heated to ~450 °C to ~700 °C by a button heater while boron was deposited from an electron beam evaporator (Focus Gmbh.) with a boron rod source (ESPI metals, 99.9999%). The deposition rate was maintained between 0.01 to 0.1 ML/min., using dual power sources to deliver 1.8-2.3 kV accelerating voltage and 1.5-1.9 A filament current. Using this setup, we obtain ~50 W incident power on a ~3 mm diameter boron rod. The flux was monitored using a faraday cup and periodic calibration on a clean Ag(111) crystal at room temperature. The boron rod was degased for > 6 hours at ~50 W heating power, until the chamber pressure was < 5.0 x 10^{-10} mBar during operation. However, depositions at pressures up to ~2 x 10^{-9} mBar showed no significant alteration in structure or morphology. The silicon capping layer for *ex-situ* analysis was deposited from an electron beam evaporator, using a solid silicon rod source (ESPI metals, 99.9999%) using 800 V accelerating voltage and ~1.8 A filament current to achieve ~15 W power incident on a ~1.5 mm rod. Degasing occurred at ~15 W for several hours, until the pressure was < 5.0 x 10^{-10} mBar. The silicon was deposited on a cold sample, immediately following retrieval from the microscope at ~40 K.

In situ characterization

STM measurements were conducted in an Omicron Nanotechnology VT-SPM at either 55 K or 300 K. All images presented are at 55 K, unless otherwise noted. STM measurements were acquired in constant current mode, using electrochemically etched W tips degassed *in situ*. In order to reduce apparent noise in some STM images, a Gaussian filter was applied with radii of 2-3 pixels (*i.e.,* much smaller than the features of interest). Simultaneous dI/dV mapping during scanning and STS spectra were acquired using the lock-in technique (10 kHz modulation, 30 mV amplitude). LEED and *in situ* AES employed a 4-grid detector (Omicron SpectraLEED), and AES was acquired with incident beam energy of 1.5 keV and a lock-in modulation of 2.0 V peak-to-peak. AES spectra were charge-corrected to the position of the elastic primary peak at 1500 eV.

Ex situ characterization

Scanning electron microscopy (SEM) and focused ion beam (FIB) milling were performed in a FEI Helios system. FIB samples were milled with a Ga^+ ion beam. TEM samples were prepared by FIB and stored under inert atmosphere. Aberration-corrected scanning transmission electron microscopy (AC-STEM) imaging and electron energy loss spectroscopy (EELS) were performed using a JEOL ARM 200F microscope equipped with a Gatan GIF 863 Tridiem spectrometer system operating at 200 kV. Care was taken to minimize the electron beam exposure to the sample, in order to reduce electron beam-induced modification of the Ag(111) substrate(*31*, *32*). High-angle annular dark field (HAADF) and annular bright field (ABF) images were sequentially acquired to provide complementary information concerning the sample

composition. The Gatan spectrometer was set to an energy dispersion of 0.5 eV/channel, in order to obtain the best energy resolution at the zero-loss peak. EELS spectra were acquired using the scanning mode to obtain a line profile spectra set to at the same energy as the zero-loss peak, with a 2.0 mm aperture and a 10 ms pixel time per 1.0 nm of the sample to increase the signal obtained from the boron (188 eV) at the interface. The DeConvEELS (*33*) software package was applied to rectify the EELS spectra by deconvolution with a zero-loss spectrum (thereby acting as a software monochromator). Ambient AFM measurements were performed on a Bruker Multimode system in Peakforce mode using silicon tips with a nominal <10 nm radius of curvature. XPS measurements were acquired in a Thermo Scientific ESCALAB 250Xi, using an electron flood gun for charge compensation. All XPS data were resolved with ~0.1 eV resolution employing a monochromated Al Kα X-ray source at ~1486.7 eV (~400 μm spot size). General core level spectra were the average of 5 scans with a 100-350 ms dwell time, using a pass energy of 15 eV. For angle-resolved XPS (AR-XPS), the sample stage was tilted with respect to the x-ray source and photoelectron detector, while single spectra were taken at each angle. AR-XPS core level spectra data as presented were taken with pass energies of 50 eV, and the results confirmed with 15 eV pass energy spectra. When using charge compensation, all core levels were charge corrected to adventitious carbon at ~284.8 eV. All subpeaks were fitted with singlets for *s* photoelectrons, using the software suite Avantage (Thermo Scientific).

Computational methods

Ab initio structure predictions were performed using the USPEX code with surface prediction module(*23*, *24*). The Ag(111) substrate was constructed by rectangular and hexagonal lattices, respectively. The lattice vectors are a=5.004 Å and b=2.889 Å for rectangular lattice and a=b=5.778 Å for hexagonal lattices. The structure searches were conducted with 6, 8, 10, 12, 14 and 16 atoms per unit cell for the hexagonal substrate; and 6, 7, 8, 10, 12, 14, 16 atoms per cell for the rectangular lattice, respectively. The thickness of the surface layer of two-dimensional (2D) boron and the vacuum were set to 3 Å and 10 Å during the searching, but allowed to change for postprocessing. To investigate the likelihood of alloy formation, a structure search was performed with the rectangular lattice by varying the number of Ag and B atoms between values of up to 8 and 16 atoms. The chemical potential for Ag and B are -2.82 eV/atom and -6.68 eV/atom, respectively. The structural relaxations used the all-electron-projector-augmented wave method (*34*) as implemented in the Vienna *ab initio* simulation package (VASP) (*35*, *36*). The exchange-correlation energy was treated within the generalized gradient approximation (GGA), using the functional of Perdew, Burke, and Ernzerhof (*37*). The cutoff energy of 450 eV and the uniform Γ-centered *k*-points grids with resolution of $2\pi \times 0.04$ Å^{-1} were used. Phonon dispersion curves and the simulated scanning tunneling microscopy (STM) images were computed with the PHONOPY package and Hive code (*38*, *39*).

We calculated the change of energy in the strain range (between -2% and 2% with an increment of 0.5%) to determine the mechanical properties of the 2D boron sheet. For a 2D sheet, using the standard Voigt notation (*40*), the elastic strain energy per unit area can be expressed as

$$\mathrm{U}(\varepsilon) = \frac{1}{2}C_{11}\varepsilon_{xx}^2 + \frac{1}{2}C_{22}\varepsilon_{yy}^2 + C_{12}\varepsilon_{xx}\varepsilon_{yy} + 2C_{66}\varepsilon_{xy}^2$$

Where C_{11}, C_{22}, C_{12}, and C_{66} are components of the elastic modulus tensor, corresponding to the second partial derivative of strain energy with respect to strain. The elastic constants can be derived by fitting the energy curves associated with uniaxial and equibiaxial strains (*41*). When

we applied this method for penta-graphene, we obtained calculated C_{11} and C_{12} as 288 GPa·nm and -32 GPa·nm, which are in good agreement with the reported values (265 and -18 GPa·nm). For the 2D boron sheet, the corresponding C_{11}, C_{22}, C_{12}, and C_{66} are 398, 170, -7, and 94 GPa·nm, respectively (from fitting to fig. S7E). The in-plane Young's modulus and Poisson's ratio can be derived from the elastic constants by (*42*)

$$E_x = \frac{C_{11}C_{22} - C_{12}C_{21}}{C_{22}},\ E_y = \frac{C_{11}C_{22} - C_{12}C_{21}}{C_{11}},\ \nu_{xy} = \frac{C_{21}}{C_{22}},\ \nu_{yx} = \frac{C_{12}}{C_{11}}$$

Therefore, the Young's modulus and Poisson's ratio are 398 GPa·nm, -0.04 in the **x** direction (i.e., parallel to the **a** vector), and 170 GPa·nm, -0.02 in the **y** direction (i.e., parallel to the **b** vector). Most strikingly, the in-plane Young's modulus in the **x** direction is comparable to or even exceeding that of graphene (340 GPa·nm) (*27*). Moreover, the 2D boron sheet has a negative C_{12}, leading to be the first 2D boron structure with negative Poisson's ratio due to the special buckled atomic configuration, similar to those recently reported in a single-layer black phosphorus (*43*) and penta-graphene (*41*).

AC-STEM images were simulated with the JEMS software package (*44*), using parameters matching the experimental conditions. An amorphous silicon capping layer (generated using a-Si Generator(*45*)) was added to the predicted structure in order to better model the contrast of the sample.

Supplementary Text

Auger electron spectroscopy

Auger Electron Spectroscopy (AES) *in situ* verified the cleanliness of the surface before deposition, and the chemical identity of the samples following STM measurements. Auger transitions respond to changes in the local chemical environment due to shifts in both the valence and core level energies (*46*, *47*). The formation of compounds generally results in shifts of at least several eV. Low atomic number elements like boron are especially susceptible to these shifts.

Representative AES spectra obtained on clean Ag(111), Ag(111) with borophene, and Ag(111) with a thicker (~4-6 ML) amorphous boron film are presented in Fig. S1A. In the clean Ag(111) spectrum, we see the characteristic Ag MNN spectrum (*47*), with sharp peaks at 351 and 356 eV and broad secondary peaks at 263 and 303 eV. Boron deposition does not noticeably modify the silver peaks, indicating there was no substantial chemical modification to the surface(*46*) (*i.e.,* alloying or compound formation). Following the deposition of 1 ML at a substrate temperature of 550 °C (red curve), the boron KLL peak is clearly observed at the expected 180 eV. Comparison with relatively thick, amorphous boron (deposited at room temperature) shows no extra peaks or peak shifts, which confirms that the measured boron KLL peak position corresponds to unreacted, pure boron (*46*).

We observed no additional peaks due to contaminants or oxygen (~500 eV, see Fig. S1B) (*47*) and we verified the absence of carbon through the ratio of the silver 266 eV and 304 eV peaks (*48*) (typical measured value of 0.42 before and after boron deposition). The presence of even slight carbon contamination would significantly distort the Ag peaks in dN/dE spectra. Furthermore, the peak shape does not change following deposition, suggesting that no carbon contamination is introduced by the boron source.

Low energy electron diffraction

Spatially averaged atomic structural data is obtained through in situ low-energy electron diffraction (LEED). In LEED, the magnitude of the reciprocal space scattering vector q is given by

$$\left|\overrightarrow{q_{hk}}\right| = \frac{1}{\left|\overrightarrow{G_{hk}}\right|}$$

where G_{hk} represents the real-space translation vector of the surface and h and k represent the indices of the diffraction spot. The sampled region of reciprocal space is inversely proportional to the electron de Broglie wavelength; therefore, higher electron energy images larger reciprocal lattice vectors (*i.e.,* smaller real space distances).

Reciprocal space structural data are also obtained by performing a fast Fourier transform (FFT) on STM images. Fig S3A and S3B show sequentially acquired topography images of the Ag(111) surface and a nearby region of striped/rectangular phase. Fig. S3C shows the superposition of FFTs on Fig. S3A and S3B, where the spots related to the Ag(111) and boron structures are highlighted in red and blue, respectively. The borophene reciprocal lattices vectors are indicated. For comparison, FFTs on the calculated structure model (Fig. 2A, 2B) are given in

Fig. S3D. This calculated pattern corresponds very well to the experimentally acquired FFT, showing the same relationships between the Ag(111) and borophene spots. Additional spots related to the atomic structure of the borophene are indicated in this model.

These FFT patterns matched the data acquired through LEED, as in Fig. S3E, which showed apparent six-fold symmetry for the borophene sheets. The strong diffraction spots circled in red are related to the Ag(111) 1×1 surface, whereas the blue spots are related to the structure of the borophene. The apparent six-fold symmetry of these additional spots results from the three possible orientation of the boron sheets (observed in STM). The additional spots are related to the Moiré pattern and buckling of the boron sheets. Lower energy LEED (68.5 eV, Fig. S3F) shows these spots more clearly. The spots highlighted in orange are due to the a* periodicity, or the formation of the striped domains. Similarly, the spots circled in purple are related to the buckling along the b* direction. In the case of the rectangular lattice, these correspond to a 1×3 reconstruction of the relaxed freestanding structure or rectangular $2\times(\sqrt{3}/2)$R30° with respect to the substrate. The spots circled in blue correspond to the short-range, rhombohedral Moiré pattern in the homogeneous phase, which results in a $\sqrt{3}\times\sqrt{3}$R30° symmetry relative to the substrate. Many of the lower *q*-space magnitude (*i.e.,* larger real-space distance) spots are somewhat less well defined, consistent with the variable periodicities of buckling in the stripe phase. We determine the buckling reconstruction parameters for the most ordered stripe patterns in the STM discussion below. Deposition at a slower rate (Fig. S3G) results in a more ordered LEED pattern and elimination of the $3\times\sqrt{3}$R30° spots due to increased conversion of the homogeneous phase to the striped phase.

Structure and morphology of the homogeneous phase

Several grains of the homogeneous phase are shown in Fig. 1D,E. Homogeneous phase islands typically exhibit truncated triangle or truncated oval (i.e., "bullet-like") shapes. No homogeneous phase islands were observed for growth at 700 °C, suggesting that high temperature and/or slow deposition enable the kinetically limited phase transformation from the homogeneous phase to the striped phase to proceed. Although the homogeneous phase islands often appear featureless at the large scale, they exhibit multiple scales of Moiré pattern, including a ~0.9 nm rhombohedral pattern, and one-dimensional Moiré patterns with ~8 nm periodicity, as in Fig. S4A,B. The 1D Moiré pattern correlates to variations in the degree of lateral distortion of the chain features in the atomic-scale structure (fig. S4B). Concurrent with this chain structure, bias dependent imaging reveals additional structure connecting adjacent chains (Fig. S4C), which implies that the buckled atomic chain structure typically observed likely only captures the structure of the highest protruding features. We frequently observe 1D line defects, as in Fig. S4A-D. These defects sometimes appear as anti-phase boundaries in terms of the inter-chain lateral distortions (*i.e.,* the direction of the lateral distortions is opposite), which may result in strain relief or serve to nucleate the proposed phase transition from homogeneous to striped phase.

Striped phase structure and morphology

Uniaxial stripe structures are common in 2D material heteroepitaxy (*22*, *49*), resulting from dissimilar symmetries, strain relaxation, and inhomogeneous substrate interactions. Growth at 700 °C results in striped phase islands with a ~8 nm rhombohedral Moiré pattern (Fig. S5A). However, there are always regions with the rectangular lattice within striped phase domains,

which appear as the dark regions in Fig. S5A. The Moiré pattern continues over these rectangular lattice regions, but is distorted translationally (shown by the jog in periodicity marked with a blue line) and rotationally (marked by the misalignment of the white lines). The atomic scale structure within the Moiré striped regions is shown in Fig. S5B. In addition to the bucking of adjacent stripe features relative to their neighbors, we observe additional displacement (*i.e.,* depressions) induced by the large-scale Moiré. Similar buckling is associated with the superposition of domains with dissimilar symmetry (*50*). The FFT inset demonstrates the emergence of spots that correspond to those highlighted in orange and purple in Fig. S3F.

The rhombohedral Moiré pattern can be reproduced (Fig. S5C) by superimposing a borophene lattice (blue spheres) upon the Ag(111) surface (green spheres), assuming no tilt from the theoretically calculated orientation and a 4% in-plane compressive strain along the **a** direction. The insets show magnified regions of the Moiré pattern. In the apparent crest (lighter regions, shown in lower inset), we see alignment between the B atoms and the hollow sites, whereas the valleys in the Moiré pattern (darker regions, shown in upper inset) show alignment with the Ag atoms. This suggests that the adsorption side of the boron atoms drives the corrugation of the striped phase. In BN growth on various transition metal substrates, boron is known to preferentially adsorb in the hollow sites of the hexagonal surface (*20*, *51*), which is consistent with this analysis.

At a growth temperature of 550 °C (Fig. S5D), we observed regions of Moiré striped phase coincident with less regularly striped domains, rotated by 120°. Despite this incongruity in stripe pattern and the rotation, the domain boundary remains relatively featureless. The congruity between these phases at the atomic scale becomes apparent in Fig. S5E. Regions of the rectangular lattice coincide smoothly with the striped structure (indicated by white arrow). The rectangular and Moiré striped regions appear to bond readily with one another (indicated by green arrow), revealing connected features with three-fold symmetry at the interface. Nearby, several unit cells of the rectangular lattice are observed to flow smoothly into the Moiré striped phase. The structure of the striped phase regions near large gaps between the domains (indicated by blue arrow) suggests that the striped phase consists of a more highly buckled lattice. Comparison with the overlaid structure models on the rectangular lattice region (upper left) and the striped phase region (lower right) shows that ~5% strain along the **a** direction provides coincidence with the striped phase lattice, consistent with the Moiré pattern simulated in fig. S5C. Comparison between the overlaid structure model and the striped phase allow us to define a transformation matrix

$$\begin{pmatrix} a_r^* \\ b_r^* \end{pmatrix} = \begin{pmatrix} 15/2 & 3/2 \\ 0 & 1 \end{pmatrix} \begin{pmatrix} a_i^* \\ b_i^* \end{pmatrix}$$

where the subscripts *i* and *r* denote the initial and reconstructed lattice vectors, respectively.

Certain features in STM provide further evidence for conversion from the homogeneous phase to the striped phase. Figure S5F shows a region in which a grain of striped phase is divided into multiple domains. The smaller domain exhibits an overall shape consistent with that typically found in the homogeneous phase. Additionally, the shape of the striped phase domains

often closely resembles those of the homogeneous phase (Figs. 1F,G), but is more compact in size.

Scanning transmission electron microscopy/electron energy loss spectroscopy

The HAADF operation mode works well for materials with different Z number because the intensity dependence on atomic number is close to $Z^{3/2}$ (*52*). In Figure S10A, a HAADF-STEM image shows atomic positions of silver. However, light elements such as boron, carbon or oxygen are not detectable by HAADF imaging. In the JEOL ARM200F microscope bright field (BF) images can be collected at the same time as the HAADF images are recorded. The BF detector in the microscope has been configured so that it can register light atoms (extremely weak scattering) using the circular beam stopper in the center of the optical axis (*29*). Under these conditions, annular bright field (ABF) and HAADF images can be recorded at the same time as well. ABF imaging has proven to be an effective mean of visualization for lighter atoms (*29*), such as boron as shown in Figure S10b.

A STEM-EELS analysis is used to probe the boron signal, the line scan is shown in Figure S11A. An intensity profile extracted from the EELS spectrum at the B K edge (~188 eV) is correlated with the HAADF image intensity profile of the same scanned region. During the acquisition, the spectrum of the B K edge intensity is recorded simultaneously with the HAADF signal. The significant increase in the B K edge intensity profile observed at the interface between silver/boron/silicon is shown in Figure S11B (red curve, boron deconvolution shown in purple curve). Additional peaks between 100 and 150 eV are associated with silicon and silicon oxide (*53*), and match those in the capping layer (blue curve).

X-ray photoelectron spectroscopy

Survey spectra on silicon-capped samples (Fig. S13A) show peaks for Ag, B, Si, O, and adventitious C (which is always present following ambient exposure). Cross-sectional STEM shows an average Si capping layer thickness of 2-4 nm, comparable to the escape depth for photoelectrons in XPS. This allows us to probe the chemistry of the Ag substrate, boron film, and Si capping layer simultaneously.

Because pure boron slowly oxidizes under ambient conditions (*54*), borophene samples capped with silicon were compared with ambient-exposed borophene to determine the oxidation state of the material as deposited, shown in Fig. 3D. The silicon capped sample exhibits one principal feature after 2 days, consistent with successful protection of the underlying borophene. This main peak displays an asymmetric shape composed of two components at 188.2 and 188.8 eV. These are consistent with B-B bonding in pure boron species (*54-56*) under two slightly different chemical environments (such as boron atoms interacting directly with the substrate versus those buckled upwards). When directly exposed to ambient (i.e., no cap), we observe peaks at 187.9, 188.3, and 192.1 eV. This broadening of the principal boron peaks, as well as a partial shift towards lower binding energies, is typical of boron oxidation, as is the peak at 192.4 eV, which likely corresponds to a sub-stoichiometric oxide (*54*). Following 3 weeks of ambient exposure, the capped sample exhibits similar peaks at 187.5, 189, and 192.4 eV. The silicon capping layer was fully oxidized, as shown by the Si 2p peak doublet at ~103 eV associated with oxide formation on amorphous films (Fig. S13B) (*56*). C 1s core level spectra (fig. S13C) showed only adventitious C, indicating that the substrate and B source are not contaminated with

C (which would otherwise result in additional peaks for B-C bonds). We observed no splitting of the Ag 3d peaks (fig. S13D), which would indicate B-Ag compound formation.

Additional angle-resolved XPS data are presented in Fig. S13E, showing the peak component height versus angle. These data revealed the same trends observed in Fig. 3E, thus supporting our proposed structure model.

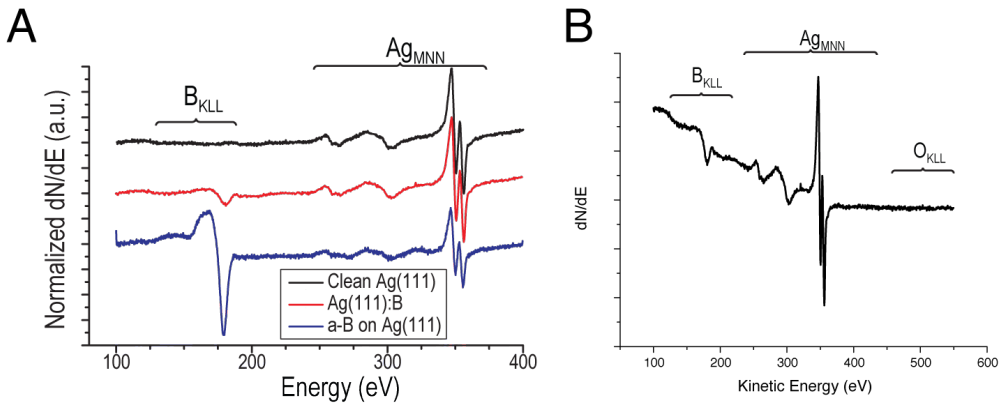

Fig. S1. Auger electron spectroscopy analysis and discussion

(A) AES spectra of clean Ag(111), borophene (~1 ML) grown at 550 °C, and a thicker (~4 ML) amorphous boron film. **(B)** AES spectrum of borophene film with extended range, demonstrating the absence of impurity peaks.

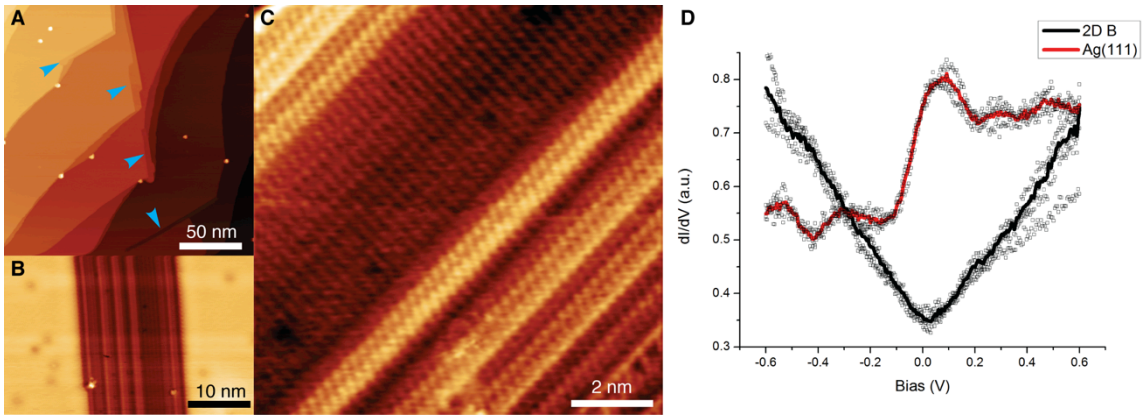

Fig. S2. Formation of borophene nanoribbons

STM topography images of low-flux *(~0.02 ML/min),* low-coverage deposition at 550 °C showing **(A)** large scale region with several nanoribbons at step edges (blue arrows) and within terraces (blue arrow). (V_{sample} = 1.0 V, I_t = 200 pA) **(B)** Magnified image demonstrating the internal striped structure of the nanoribbons. (V_{sample} = 0.2 V, I_t = 500 pA) **(C)** Atomic scale structure of the nanoribbons, demonstrating their structural correspondence with the extended 2D stripe phase sheets. (V_{sample} = -0.1 V, I_t = 5 nA). **(D)** STS point spectra obtained on the rectangular lattice phase regions of the striped boron nanoribbons, demonstrating their metallic characteristics.

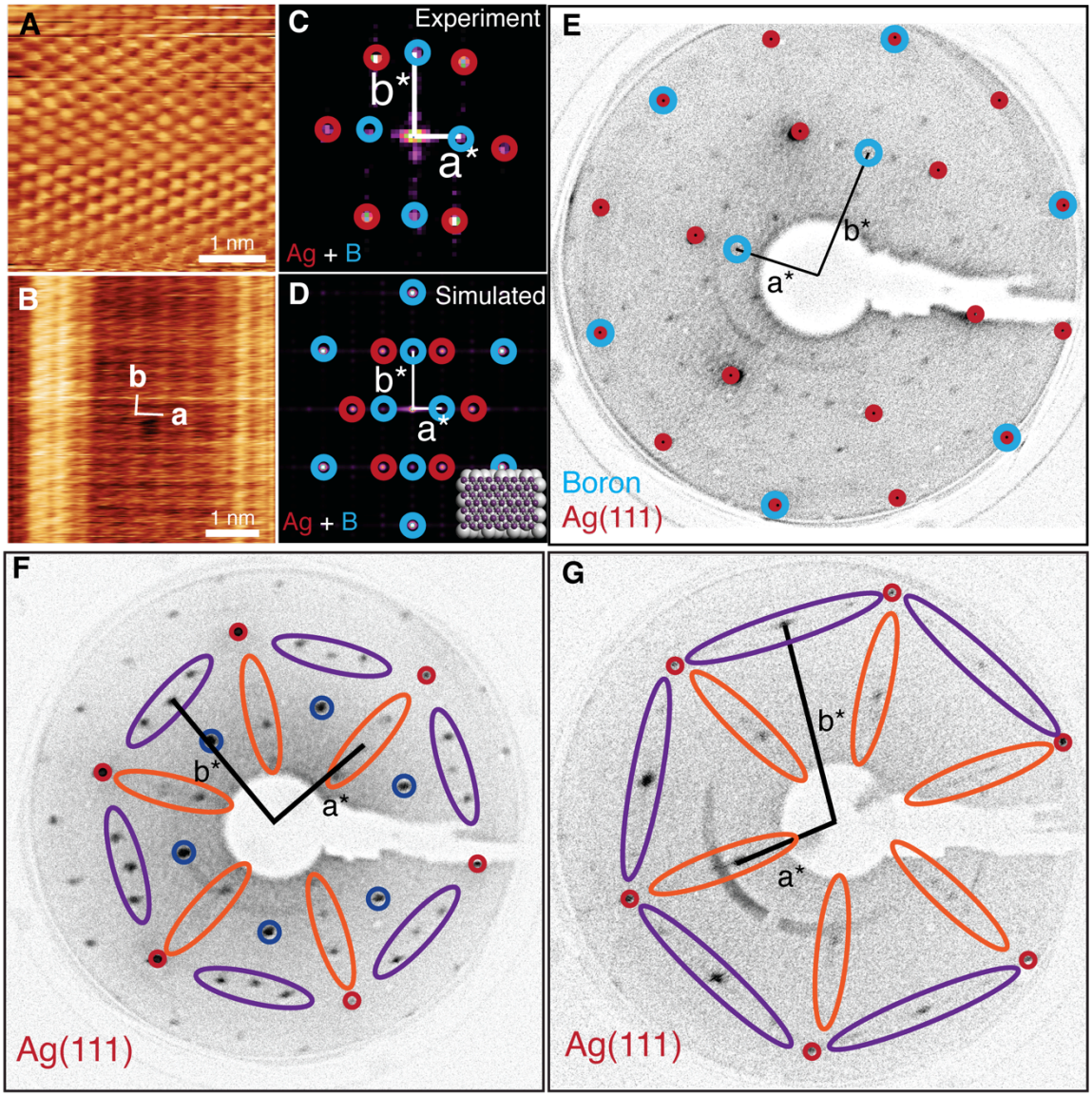

Fig. S3. Structure analysis and low energy electron diffraction of borophene

Sequentially acquired STM topography of **(A)** Ag(111) lattice (V_{sample} = 25 mV, I_t = 1.0 nA) and **(B)** borophene (V_{sample} = 50 mV, I_t = 2.0 nA). **(C)** Superimposed fast Fourier transformations (FFTs) of **(A)** and **(B)**. **(D)** FFT of low-energy monolayer structure model given in Fig. 2 (shown inset). This FFT is not scaled to **(C)**, comparison is made relative to the Ag(111) spots (circled in red). **(E,F,G)** LEED patterns acquired at **(E)** 120 eV, **(F)** 68.5 eV, and **(G)** 68.5 eV. **(E)** and **(F)** were acquired sequentially on the same 550°C growth, whereas **(G)** was acquired on a lower deposition rate growth at 700 °C.

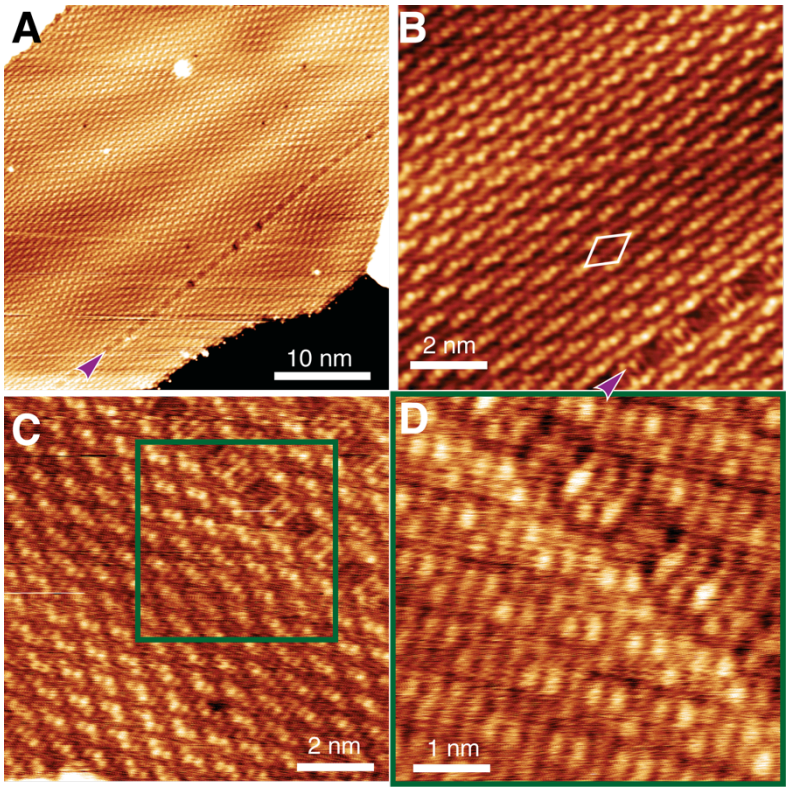

Fig. S4. Detailed structure and morphology of the homogeneous phase

STM topography images of **(A)** Atomically resolved homogeneous phase demonstrating chain morphology, line defect, and Moiré structure (V_{sample} = 0.1 V, I_t = 500 pA). **(B)** Atomically resolved image of typical chain structure. The short-range Moiré pattern is highlighted with a white rhombus (V_{sample} = 0.1 V, I_t = 3.0 nA). **(C,D)** Atomically resolved images of **(C)** typical chain structure (V_{sample} = 0.1 V, I_t = 1.0 nA) and **(D)** magnified region (from green square) demonstrating bias-dependent changes in contrast which reveal structural relationships between the chains (V_{sample} = -20 mV, I_t = 1.0 nA).

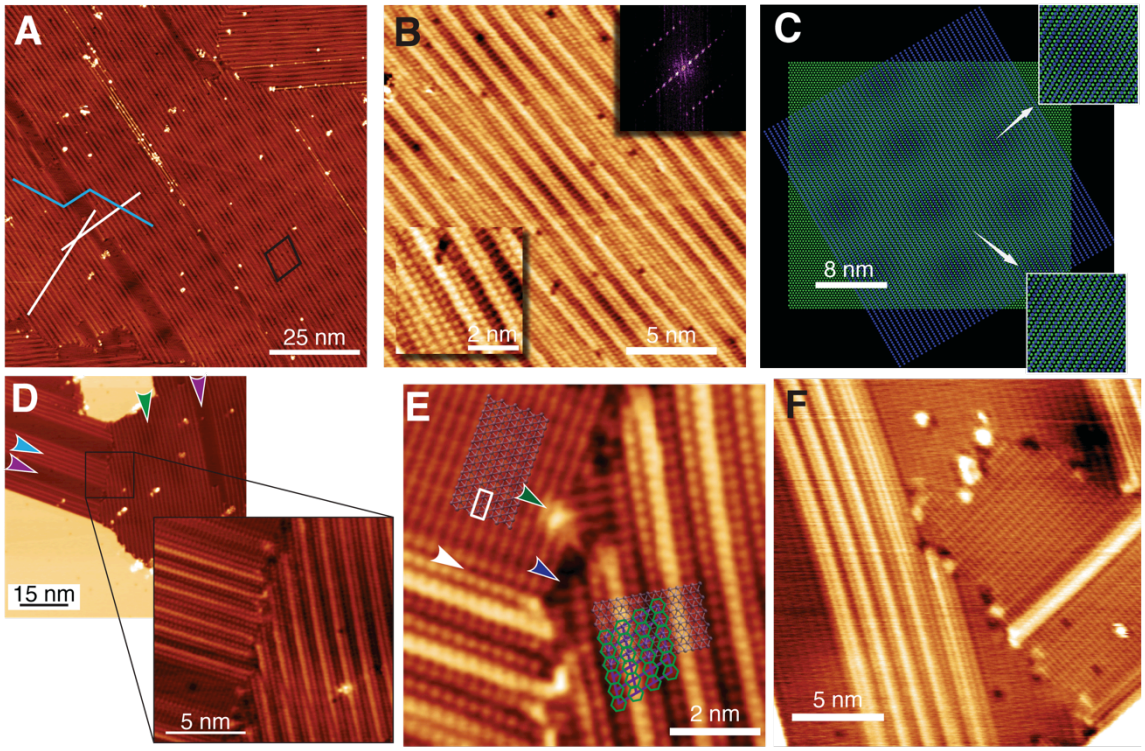

Fig. S5. Detailed structure and morphology of striped phase

(A) STM topographic image of the interior of a borophene sheet grown at 700 °C, demonstrating rhombohedral Moiré pattern and regions of non-buckled rectangular lattice (V_{sample} = 1.2 V, I_t = 500 pA). **(B)** Atomic resolution image of a borophene striped sheet. *Upper inset:* FFT of **(B)**. *Lower inset*: high resolution image (both images at V_{sample} = 0.1 V, I_t = 500 pA). **(C)** Moiré pattern generated from the superposition of a strained borophene lattice (4% compressive along the **a** direction) on the Ag(111) plane. The insets show magnified views of the Moiré trough and crest, detailing the different adsorption sides in each. **(D)** Images of 550 °C growth, detailing the interfacial relationship between a striped phase domain with periodic buckling, and a striped phase domain with nearly complete stripe coverage (V_{sample} = 0.2 V, I_t = 3.0 nA). Purple arrows denote rectangular lattice regions, the blue arrow denotes a non-Moiré striped phase, and the green arrow denotes a Moiré striped phase. **(E)** Atomic resolution image detailing the limited structural coherency and common structural motifs between the rectangular and striped phases (V_{sample} = 0.1 V, I_t = 3.0 nA). **(F)** Atomically resolved image of striped phase region generated by the coalescence of multiple islands. The smaller striped domain exhibits a "bullet-like" shape characteristics of the homogeneous phase (V_{sample} = 0.1 V, I_t = 1.0 nA).

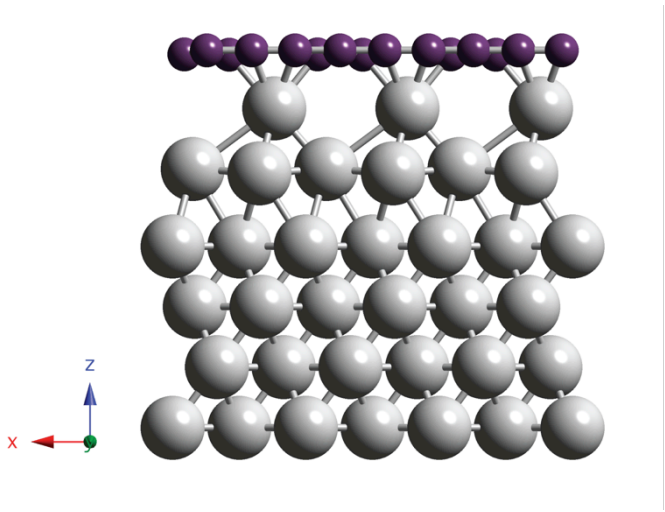

Fig. S6. Computational studies of alloying or boride formation

Sample structure model for boron-rich alloy (*i.e.,* matching the experimental conditions), showing the restructuring of the near-surface silver region and segregation of the boron to the surface.

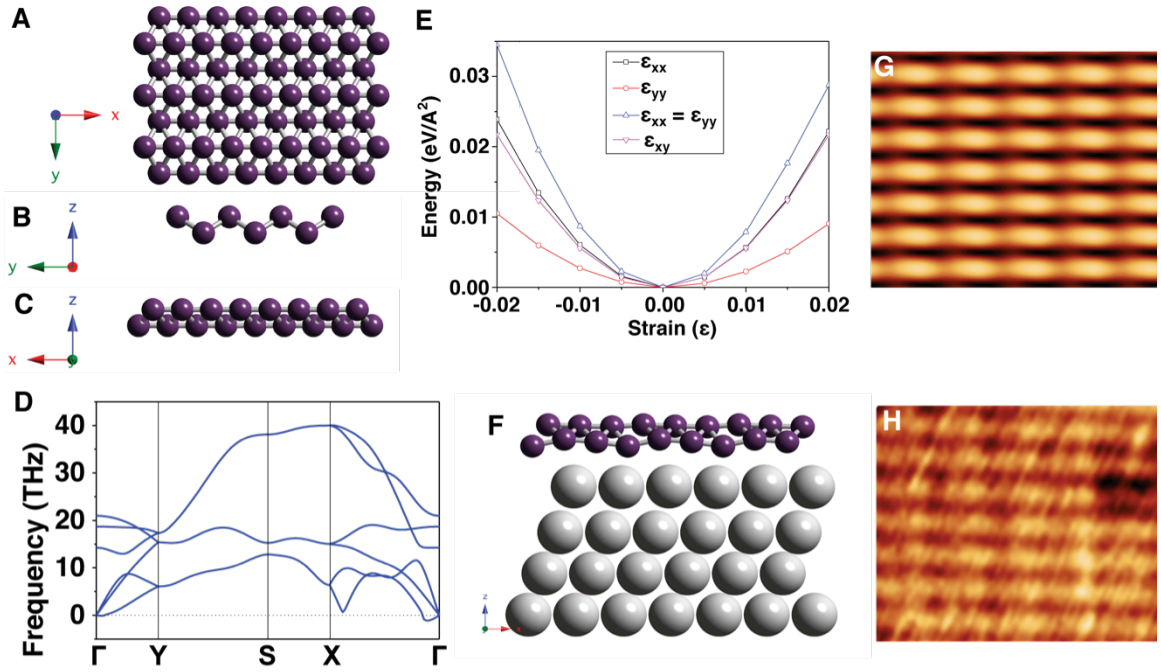

Fig. S7. Computational monolayer structures

(A,B,C) top, front, and side views of the atomic structure of a free-standing borophene sheet. Structural relaxation results in decreased corrugation along the **a** direction, which results in a decreased unit cell size. The resulting lattice parameters are **a** = 0.1617 nm (corresponding to ~1/3 the lattice parameter in Fig. 2A,B) and **b** = 0.2865 nm. **(D)** Phonon dispersion of freestanding borophene sheet. The small imaginary frequencies near the Γ point are consistent with instability against long-wavelength transversal waves(*57*). This instability can be fixed by defects, such as ripples or grain boundaries, which do not allow these waves by limiting the size of boron sheets. **(E)** Calculated strain vs. energy for freestanding borophene sheet. **(F)** Structure model corresponding to a metastable borophene sheet, slightly distorted with respect to the most stable structure (Fig. 2A). **(G)** Simulated (V_{sample} = 0.1 V, I_t = 3.0 nA) and **(H)** experimental (V_{sample} = 0.1 V, I_t = 3.0 nA) STM topography images.

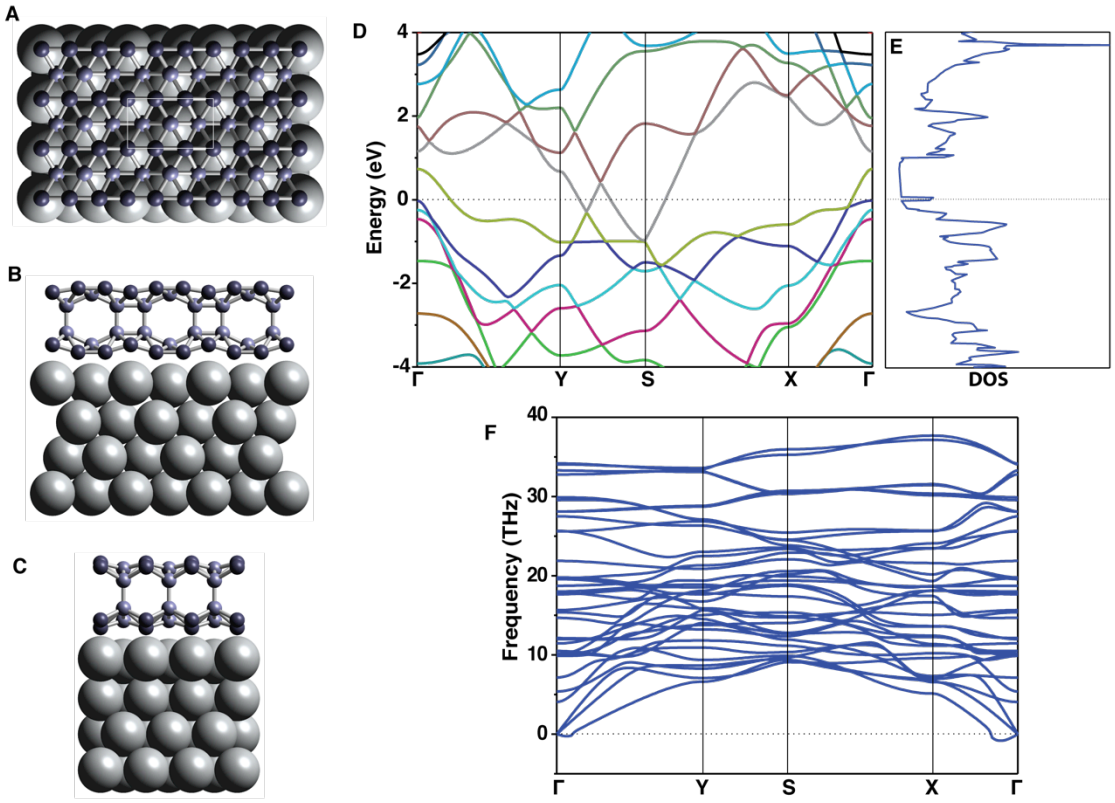

Fig. S8. Computational bilayer structures

(A,B,C) Top, side, and frontal views of bilayer borophene structure. Structural relaxation of the freestanding sheet results in lattice parameters of **a** = 0.490 nm and **b** = 0.288 nm. **(D)** Calculated electronic band structure for freestanding, bilayer borophene and **(E)** associated electronic density of states, both of which show metallic characteristics. **(F)** Calculated phonon dispersion for the bilayer structure. The small region of imaginary frequencies near the gamma point is interpreted as in Fig. S7.

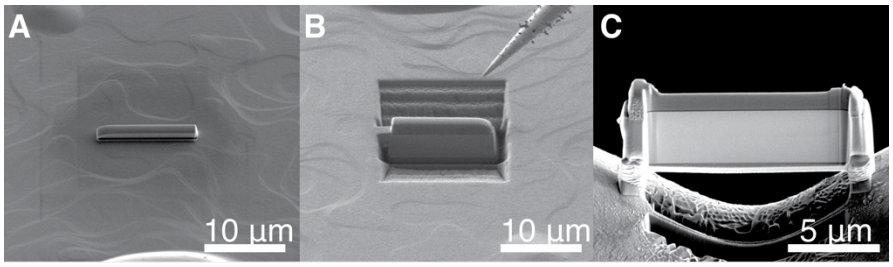

Fig. S9. Cross-sectional AC-STEM sample prep

SEM images acquired during focused ion beam (FIB) milling of a cross-sectional sample for STEM. Once a suitably flat region is selected, a protective platinum cap/handle is deposited *in situ* (A). The region surrounding the sample is then milled out using the Ga^+ ion beam (B). Immediately prior to severing the last connection of the sample to the substrate, the sample is welded to the tungsten probe via platinum deposition. Once the sample is separated from the substrate, it is transferred via the tungsten probe to the sample post of a semi-circular copper grid. The sample is welded to the post with platinum deposition, separated from the tungsten probe, and successively thinned to < 30 nm by the ion beam (C).

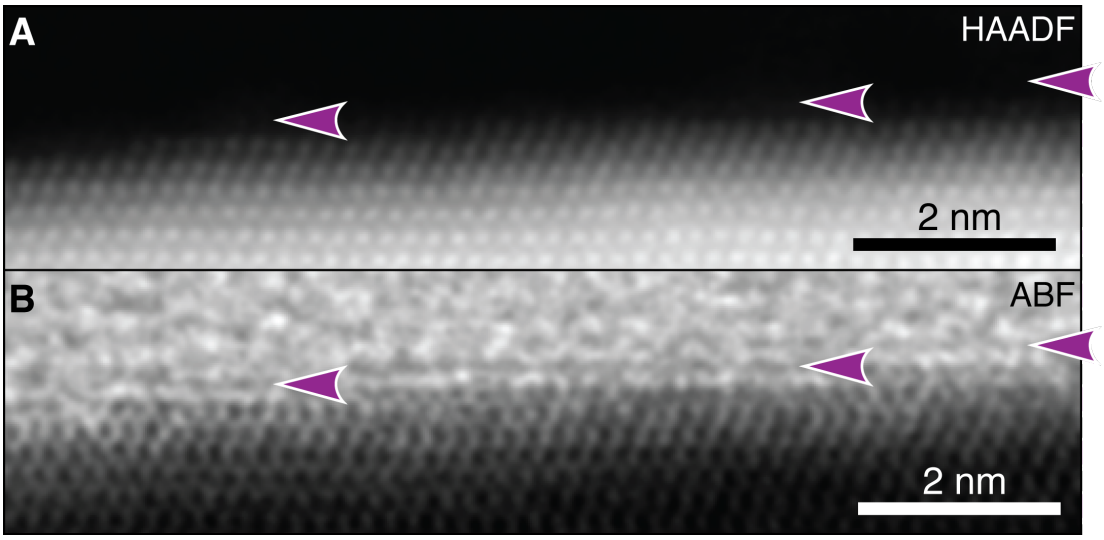

Fig. S10. Additional AC-STEM data

AC-STEM images acquired on an atomically stepped surface region with (A) HAADF and (B) ABF detectors. The purple arrows are located at the same relative positions between images, and indicate the presence of light elemental planar features, which we identify as borophene.

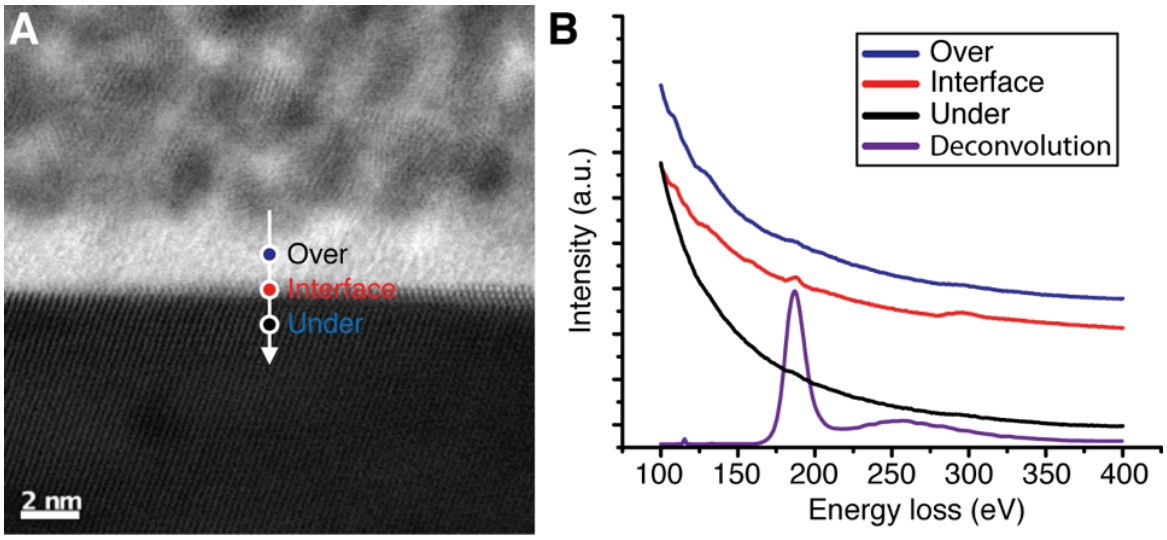

Fig. S11. STEM EELS

(A) AC-STEM survey image, with the location of the EELS line profile indicated. (B) Plot of EELS spectra from the regions indicated in (A). The interface spectrum (red) shows that a strong boron peak (188 eV)(*55*) is localized to the area near the interface, as confirmed by the deconvoluted boron peak (purple) (*33*). These spectra show that the boron is confined to the interface between the Ag(111) substrate and the Si capping layer.

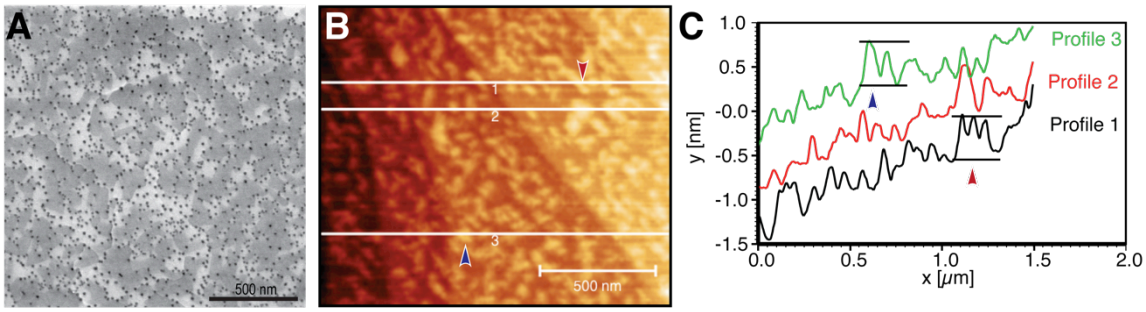

Fig. S12. Additional *ex situ* characterization of borophene

(A) SEM image of the borophene sheets after ambient exposure. The island features observed in STM persist and demonstrate significant contrast. The small dark features are attributed to boron nanoparticles, and may appear larger than in STM due to charging effects. (B) Ambient peak-force mode AFM image of borophene sheets. Based on the island morphologies, we identify striped phase (red arrow) and homogeneous phase islands (blue arrow). (C) AFM line profiles extracted from (B), showing heights of ~0.38 nm for the striped phase island (red arrow) and ~0.44 nm for the homogeneous phase (blue arrow). These step heights may deviate from theoretical predictions due to tip-sample interactions and the partial oxidation of the sheets, but are essentially consistent with both theoretical predictions and STEM observations.

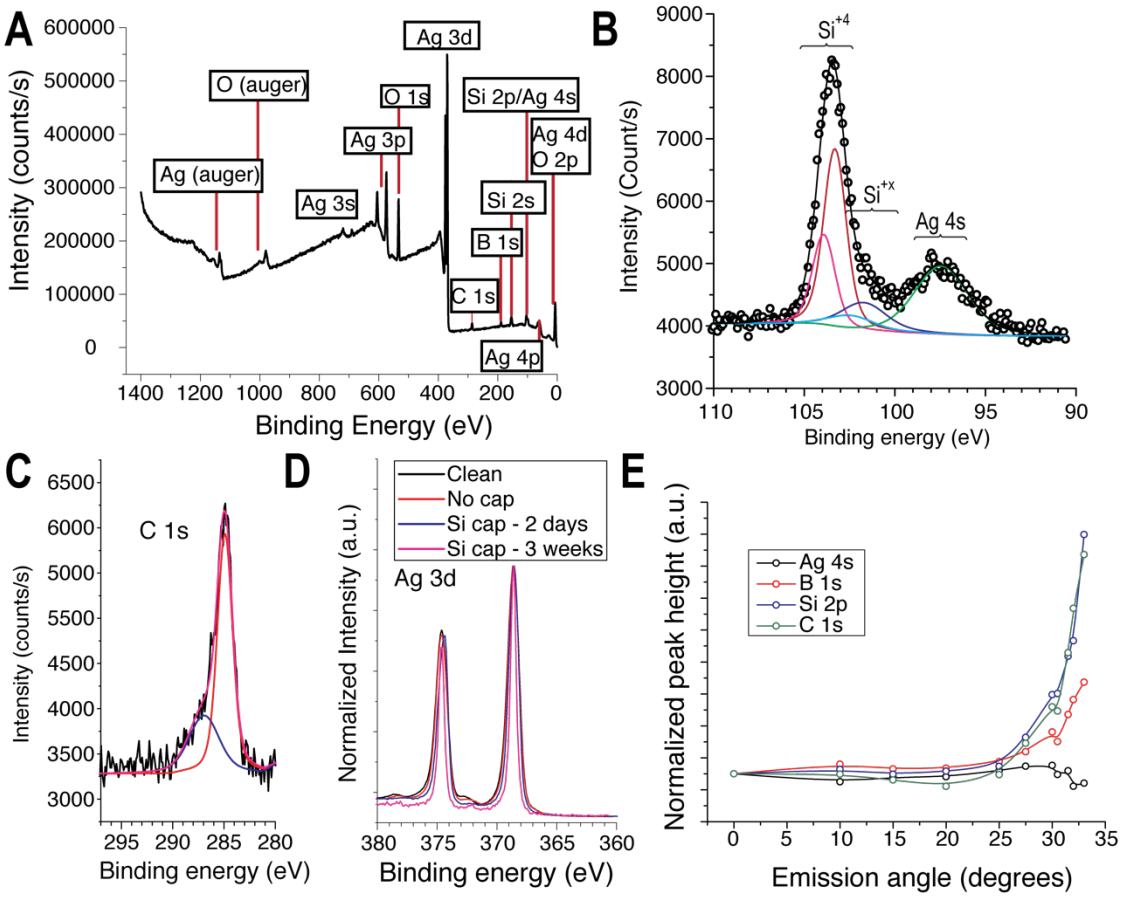

Fig. S13. Additional XPS analysis

(A) XPS survey spectrum, demonstrating the presence of Ag, B, Si, C, and O. (B) Si 2p core level data, demonstrating the presence of the almost fully oxidized amorphous silicon (~103 eV) capping layer adjacent to the Ag 4s peak. (C) C 1s core level spectrum, demonstrating the absence of any peaks besides adventitious carbon. (D) Ag 3d core level spectra, showing the silver peaks are unaltered by the B and Si cap deposition. (E) Angle-resolved XPS data showing normalized component peak heights for the species present.

References and Notes

1. T. Ogitsu, E. Schwegler, G. Galli, β-Rhombohedral boron: At the crossroads of the chemistry of boron and the physics of frustration. *Chem. Rev.* **113**, 3425–3449 (2013). Medline doi:10.1021/cr300356t

2. B. Douglas, S.-M. Ho, *Structure and Chemistry of Crystalline Solids* (Springer Science & Business Media, New York, 2007).

3. A. R. Oganov, J. Chen, C. Gatti, Y. Ma, Y. Ma, C. W. Glass, Z. Liu, T. Yu, O. O. Kurakevych, V. L. Solozhenko, Ionic high-pressure form of elemental boron. *Nature* **457**, 863–867 (2009). Medline doi:10.1038/nature07736

4. H.-J. Zhai, B. Kiran, J. Li, L.-S. Wang, Hydrocarbon analogues of boron clusters—planarity, aromaticity and antiaromaticity. *Nat. Mater.* **2**, 827–833 (2003). Medline doi:10.1038/nmat1012

5. A. P. Sergeeva, I. A. Popov, Z. A. Piazza, W. L. Li, C. Romanescu, L. S. Wang, A. I. Boldyrev, Understanding boron through size-selected clusters: Structure, chemical bonding, and fluxionality. *Acc. Chem. Res.* **47**, 1349–1358 (2014). Medline doi:10.1021/ar400310g

6. H.-J. Zhai, Y. F. Zhao, W. L. Li, Q. Chen, H. Bai, H. S. Hu, Z. A. Piazza, W. J. Tian, H. G. Lu, Y. B. Wu, Y. W. Mu, G. F. Wei, Z. P. Liu, J. Li, S. D. Li, L. S. Wang, Observation of an all-boron fullerene. *Nat. Chem.* **6**, 727–731 (2014). Medline

7. Z. A. Piazza, H. S. Hu, W. L. Li, Y. F. Zhao, J. Li, L. S. Wang, Planar hexagonal B(36) as a potential basis for extended single-atom layer boron sheets. *Nat. Commun.* **5**, 3113 (2014). Medline doi:10.1038/ncomms4113

8. I. Boustani, Systematic ab initio investigation of bare boron clusters: Determination of the geometry and electronic structures of B_n (n= 2–14). *Phys. Rev. B* **55**, 16426–16438 (1997). doi:10.1103/PhysRevB.55.16426

9. H. Tang, S. Ismail-Beigi, Novel precursors for boron nanotubes: The competition of two-center and three-center bonding in boron sheets. The competition of two-center and three-center bonding in boron sheets. *Phys. Rev. Lett.* **99**, 115501 (2007). Medline doi:10.1103/PhysRevLett.99.115501

10. X.-F. Zhou, X. Dong, A. R. Oganov, Q. Zhu, Y. Tian, H.-T. Wang, Semimetallic two-dimensional boron allotrope with massless Dirac fermions. *Phys. Rev. Lett.* **112**, 085502 (2014). doi:10.1103/PhysRevLett.112.085502

11. K. C. Lau, R. Pandey, Stability and electronic properties of atomistically-engineered 2D boron sheets. *J. Phys. Chem. C* **111**, 2906–2912 (2007). doi:10.1021/jp066719w

12. E. S. Penev, S. Bhowmick, A. Sadrzadeh, B. I. Yakobson, *Polymorphism of Two-Dimensional Boron.* **12**, 2441–2445 (2012).

13. Y. Liu, E. S. Penev, B. I. Yakobson, Probing the synthesis of two-dimensional boron by first-principles computations. *Angew. Chem. Int. Ed.* **52**, 3156–3159 (2013). Medline doi:10.1002/anie.201207972

14. H. Liu, J. Gao, J. Zhao, From boron cluster to two-dimensional boron sheet on Cu(111) surface: Growth mechanism and hole formation. *Sci. Rep.* **3**, 3238 (2013). Medline

15. F. Liu, C. Shen, Z. Su, X. Ding, S. Deng, J. Chen, N. Xu, H. Gao, Metal-like single crystalline boron nanotubes: Synthesis and in situ study on electric transport and field emission properties. *J. Mater. Chem.* **20**, 2197 (2010). doi:10.1039/b919260c

16. H. Okamoto, Ag-B (silver-boron). *J. Phase Equilibria* **13**, 211–212 (1992). doi:10.1007/BF02667492

17. M. I. Eremets, V. V. Struzhkin, H. Mao, R. J. Hemley, Superconductivity in boron. *Science* **293**, 272–274 (2001). Medline doi:10.1126/science.1062286

18. Additional supplementary text and data are available on *Science* Online.

19. B. Kiraly, E. V. Iski, A. J. Mannix, B. L. Fisher, M. C. Hersam, N. P. Guisinger, Solid-source growth and atomic-scale characterization of graphene on Ag (111). *Nat. Commun.* **4**, 2804 (2013). doi:10.1038/ncomms3804

20. S. Berner, M. Corso, R. Widmer, O. Groening, R. Laskowski, P. Blaha, K. Schwarz, A. Goriachko, H. Over, S. Gsell, M. Schreck, H. Sachdev, T. Greber, J. Osterwalder, Boron nitride nanomesh: Functionality from a corrugated monolayer. *Angew. Chem.* **46**, 5115–5119 (2007). Medline doi:10.1002/anie.200700234

21. F. Müller, S. Hüfner, H. Sachdev, R. Laskowski, P. Blaha, K. Schwarz, Epitaxial growth of hexagonal boron nitride on Ag(111). *Phys. Rev. B* **82**, 113406 (2010). doi:10.1103/PhysRevB.82.113406

22. H. I. Rasool, E. B. Song, M. Mecklenburg, B. C. Regan, K. L. Wang, B. H. Weiller, J. K. Gimzewski, Atomic-scale characterization of graphene grown on copper (100) single crystals. *J. Am. Chem. Soc.* **133**, 12536–12543 (2011). Medline doi:10.1021/ja200245p

23. A. R. Oganov, C. W. Glass, Crystal structure prediction using ab initio evolutionary techniques: Principles and applications. *J. Chem. Phys.* **124**, 244704–244716 (2006). Medline doi:10.1063/1.2210932

24. Q. Zhu, L. Li, A. R. Oganov, P. B. Allen, Evolutionary Method for Predicting Surface Reconstructions with Variable Stoichiometry. *Phys. Rev. B* **87**, 195317 (2013). doi:10.1103/PhysRevB.87.195317

25. A. Kolmogorov, S. Curtarolo, Theoretical study of metal borides stability. *Phys. Rev. B* **74**, 224507 (2006). doi:10.1103/PhysRevB.74.224507

26. B. Feng, Z. Ding, S. Meng, Y. Yao, X. He, P. Cheng, L. Chen, K. Wu, Evidence of silicene in honeycomb structures of silicon on Ag(111). *Nano Lett.* **12**, 3507–3511 (2012). Medline doi:10.1021/nl301047g

27. C. Lee, X. Wei, J. W. Kysar, J. Hone, Measurement of the elastic properties and intrinsic strength of monolayer graphene. *Science* **321**, 385–388 (2008). Medline

28. Q. Guo *et al*., Bias dependence of apparent layer thickness and Moiré pattern on NaCl/Cu(001). *Surf. Sci.* **604**, 1820–1824 (2010). doi:10.1016/j.susc.2010.07.013

29. R. Ishikawa, E. Okunishi, H. Sawada, Y. Kondo, F. Hosokawa, E. Abe, Direct imaging of hydrogen-atom columns in a crystal by annular bright-field electron microscopy. *Nat. Mater.* **10**, 278–281 (2011). Medline doi:10.1038/nmat2957

30. J. Kliewer, R. Berndt, E. V. Chulkov, V. M. Silkin, P. M. Echenique, S. Crampin, Dimensionality effects in the lifetime of surface states. *Science* **288**, 1399–1402 (2000). Medline doi:10.1126/science.288.5470.1399

31. R. F. Egerton, P. Li, M. Malac, Radiation damage in the TEM and SEM. *Micron* **35**, 399–409 (2004). Medline doi:10.1016/j.micron.2004.02.003

32. M. José-Yacaman, C. Gutierrez-Wing, M. Miki, D. Q. Yang, K. N. Piyakis, E. Sacher, Surface diffusion and coalescence of mobile metal nanoparticles. *J. Phys. Chem. B* **109**, 9703–9711 (2005). Medline doi:10.1021/jp0509459

33. DeConvEELS, available at http://www.hremresearch.com.

34. P. E. Blöchl, Projector augmented-wave method. *Phys. Rev. B Condens. Matter* **50**, 17953–17979 (1994). Medline doi:10.1103/PhysRevB.50.17953

35. G. Kresse, J. Furthmüller, Efficiency of ab-initio total energy calculations for metals and semiconductors using a plane-wave basis set. *Comput. Mater. Sci.* **6**, 15–50 (1996). doi:10.1016/0927-0256(96)00008-0

36. G. Kresse, J. Furthmüller, Efficient iterative schemes for ab initio total-energy calculations using a plane-wave basis set. *Phys. Rev. B Condens. Matter* **54**, 11169–11186 (1996). Medline doi:10.1103/PhysRevB.54.11169

37. J. P. Perdew, K. Burke, M. Ernzerhof, Generalized gradient approximation made simple. *Phys. Rev. Lett.* **77**, 3865–3868 (1996). Medline doi:10.1103/PhysRevLett.77.3865

38. A. Togo, F. Oba, I. Tanaka, First-principles calculations of the ferroelastic transition between rutile-type and CaCl2-type SiO2at high pressures. *Phys. Rev. B* **78**, 134106–134109 (2008). doi:10.1103/PhysRevB.78.134106

39. D. E. P. Vanpoucke, G. Brocks, Formation of Pt-induced Ge atomic nanowires on Pt/Ge(001): A density functional theory study. *Phys. Rev. B* **77**, 241308(R) (2008). doi:10.1103/PhysRevB.77.241308

40. R. C. Andrew, R. E. Mapasha, A. M. Ukpong, N. Chetty, Mechanical properties of graphene and boronitrene. *Phys. Rev. B* **85**, 125428–125429 (2012). doi:10.1103/PhysRevB.85.125428

41. S. Zhang, J. Zhou, Q. Wang, X. Chen, Y. Kawazoe, P. Jena, Penta-graphene: A new carbon allotrope. *Proc. Natl. Acad. Sci. U.S.A.* **112**, 2372–2377 (2015). Medline doi:10.1073/pnas.1416591112

42. Q. Wei, X. Peng, Superior mechanical flexibility of phosphorene and few-layer black phosphorus. *Appl. Phys. Lett.* **104**, 251915–251916 (2014). doi:10.1063/1.4885215

43. J.-W. Jiang, H. S. Park, Negative poisson's ratio in single-layer black phosphorus. *Nat. Commun.* **5**, 4727 (2014). Medline doi:10.1038/ncomms5727

44. P. A. Stadelmann, *JEMS-EMS java version* (CIME-EPFL, 2014).

45. E. C. Johlin, L. Wagner, J. C. Grossman, J. Riley, D. Strubbe, “Amorphous Silicon Generator” (Nanohub, 2011), doi:10.4231/D37940V61.

46. J. C. Rivière, Auger electron spectroscopy. *Contemp. Phys.* **14**, 513–539 (2006). doi:10.1080/00107517308210772

47. *Handbook of Auger Electron Spectroscopy: A Book of Reference Data for Identification and Interpretation in Auger Electron Spectroscopy* (Physical Electronics, Chanhassen, MN, 1995).

48. H. A. Engelhardt, D. Menzel, Adsorption of oxygen on silver single crystal surfaces. *Surf. Sci.* **57**, 591–618 (1976). doi:10.1016/0039-6028(76)90350-2

49. F. Bianchini, L. L. Patera, M. Peressi, C. Africh, G. Comelli, Atomic scale identification of coexisting graphene structures on Ni(111). *J. Phys. Chem. Lett.* **5**, 467–473 (2014). Medline doi:10.1021/jz402609d

50. S. Bengió, V. Navarro, M. A. González-Barrio, R. Cortés, I. Vobornik, E. G. Michel, A. Mascaraque, Electronic structure of reconstructed Au(100): Two-dimensional and onedimensional surface states. *Phys. Rev. B* **86**, 045426 (2012). doi:10.1103/PhysRevB.86.045426

51. M. Corso, W. Auwärter, M. Muntwiler, A. Tamai, T. Greber, J. Osterwalder, Boron nitride nanomesh. *Science* **303**, 217–220 (2004). Medline doi:10.1126/science.1091979

52. S. J. Pennycook, P. D. Nellist, *Scanning Transmission Electron Microscopy* (Springer Science & Business Media, New York, NY, 2011).

53. O. Lichtenberger, R. Schneider, J. Woltersdorf, Analyses of EELS fine structures of different silicon compounds. *Phys. Status Solidi, A Appl. Res.* **150**, 661–672 (1995). doi:10.1002/pssa.2211500209

54. Y. Wang, J. Fan, M. Trenary, Surface chemistry of boron oxidation. 1. Reactions of oxygen and water with boron films grown on tantalum (110). *Chem. Mater.* **5**, 192–198 (1993). doi:10.1021/cm00026a007

55. T. T. Xu, J.-G. Zheng, Wu, A. W. Nicholls, J. R. Roth, D. A. Dikin, R. S. Ruoff, Crystalline boron nanoribbons. Synthesis and characterization. *Nano Lett.* **4**, 963–968 (2004). doi:10.1021/nl0498785

56. J. F. Moulder, W. F. Stickle, P. E. Sobol, K. D. Bomben, *Handbook of X-ray Photoelectron Spectroscopy* (Physical Electronics, Chanhassen, MN, 1995).

57. H. Şahin, S. Cahangirov, M. Topsakal, E. Bekaroglu, E. Akturk, R. T. Senger, S. Ciraci, Monolayer honeycomb structures of group-IV elements and III-V binary compounds: First-principles calculations. *Phys. Rev. B* **80**, 155453 (2009). doi:10.1103/PhysRevB.80.155453